



Research Repository UCD

Title	Quantitative comparison of closed-loop and dual harmonic Kelvin probe force microscopy techniques
Authors(s)	Kilpatrick, J. I., Collins, Liam, Weber, Stefan A. L., Rodriguez, Brian J.
Publication date	2018-12-28
Publication information	Kilpatrick, J. I., Liam Collins, Stefan A. L. Weber, and Brian J. Rodriguez. "Quantitative Comparison of Closed-Loop and Dual Harmonic Kelvin Probe Force Microscopy Techniques." AIP Publishing, December 28, 2018. https://doi.org/10.1063/1.5025432 .
Publisher	AIP Publishing
Item record/more information	http://hdl.handle.net/10197/10145
Publisher's version (DOI)	10.1063/1.5025432

Downloaded 2025-12-04 22:47:33

The UCD community has made this article openly available. Please share how this access benefits you. Your story matters! (@ucd_oa)



© Some rights reserved. For more information

Quantitative comparison of closed-loop and dual harmonic Kelvin probe force microscopy techniques

Jason I. Kilpatrick,^{1,a)} Liam Collins,² Stefan A. L. Weber,^{3,4} and Brian J. Rodriguez^{1,5,a)}

¹Conway Institute of Biomolecular and Biomedical Research, University College Dublin, Belfield, Dublin 4, Ireland

²Center for Nanophase Materials Sciences, Oak Ridge National Laboratory, Oak Ridge, Tennessee 37831, USA

³Max Planck Institute for Polymer Research, 55128 Mainz, Germany

⁴Department of Physics, Johannes Gutenberg University, 55128 Mainz, Germany

⁵School of Physics, University College Dublin, Belfield, Dublin 4, Ireland

(Received 9 February 2018; accepted 26 November 2018; published online 28 December 2018)

Kelvin probe force microscopy (KPFM) is a widely used technique to map surface potentials at the nanometer scale. In traditional KPFM, a feedback loop regulates the DC bias applied between a sharp conductive probe and a sample to nullify the electrostatic force (closed-loop operation). In comparison, open-loop techniques such as dual harmonic KPFM (DH-KPFM) are simpler to implement, are less sensitive to artefacts, offer the unique ability to probe voltage sensitive materials, and operate in liquid environments. Here, we directly compare the two techniques in terms of their bandwidth and sensitivity to instrumentation artefacts. Furthermore, we introduce a new correction for traditional KPFM termed “setpoint correction,” which allows us to obtain agreement between open and closed-loop techniques within 1%. Quantitative validation of DH-KPFM may lead to a wider adoption of open-loop KPFM techniques by the scanning probe community. *Published by AIP Publishing.*
<https://doi.org/10.1063/1.5025432>

I. INTRODUCTION

Atomic force microscope (AFM) based Kelvin probe force microscopy (KPFM) is an enabling technique which allows surface potential mapping at the nanometer scale. The contact potential difference (CPD) measured by KPFM can be used to fully quantify a sample’s local electronic properties (e.g., work function) under certain conditions (e.g., vacuum), provided the influence of the environment is minimized and the tip properties are known.¹ More generally, AFM based KPFM in ambient environments may be influenced by sample preparation (e.g., surface oxidation or adsorbed dielectric layers²), by the environment (e.g., humidity³), and also by instrumentation (e.g., electronic offsets and electronic cross talk) as well as probe geometry.^{4,5} These effects combine to make traditional KPFM in ambient environments an accurate and useful technique for relative surface potential mapping, but it is often difficult to obtain the true electronic properties of the system.^{6,7}

Traditional KPFM is a closed-loop KPFM (CL-KPFM) technique where a feedback loop is used to apply a DC bias to compensate the electrostatic force between a tip and a sample.⁸ Open-loop KPFM (OL-KPFM) techniques are increasingly being adopted as feedback-free methods,^{7,9,18–20,10–17} eliminating the need for the application of a DC bias⁷ and enabling the mapping of voltage-sensitive materials^{9,15,21,22} and surface potentials in liquid environments.^{10–12,16,17,23–25} These techniques are also of interest for their reduced sensitivity to electronic offsets and electronic cross talk instrumentation

issues,^{4,7,32–35,13,22,26–31} which can affect both OL- and CL-KPFM operation to varying degrees.³⁵ Dual harmonic KPFM (DH-KPFM) is one example of OL-KPFM which has been utilized to measure surface potential^{7,9–12,15,16,25,35,36} in ultra-high vacuum,^{9,36} air,^{7,15,35} and liquid^{10–12,16,25} environments.

Here we present a rigorous and quantitative comparison of traditional KPFM (lift mode, off-resonance) with DH-KPFM using a commercial AFM system. Previously we have demonstrated that traditional KPFM and DH-KPFM obtain the same potential difference between copper and graphene surfaces, but a global offset was observed between the two techniques.⁷ Here we demonstrate that by ruling out electronic cross talk and applying corrections for electronic offsets, the difference between the techniques can be reduced from 73 mV (34%) to 45 mV (17%). We also introduce a new type of correction (“setpoint offset”) for traditional KPFM which minimizes both the distance and bias dependence of the system, allowing for more accurate CPD values to be obtained. Once all necessary corrections have been quantified and applied, the CPD in air between a metal coated AFM probe and a highly oriented pyrolytic graphite (HOPG) sample is recorded and compared using traditional KPFM and DH-KPFM techniques and agreement within 2 mV (1%) is obtained. By demonstrating the quantitative agreement between traditional KPFM and DH-KPFM, the latter technique may become more widely adopted in the emerging field of liquid KPFM.³⁷

II. BASIC PRINCIPLES OF KPFM

A. KPFM

In all KPFM-based techniques, a voltage is applied between a conductive AFM probe and a sample, $V_{probe} = V_{dc}$

^{a)}Authors to whom correspondence should be addressed: jason.kilpatrick@ucd.ie and brian.rodriguez@ucd.ie

+ $V_{ac} \sin(\omega t)$, where V_{ac} is an AC voltage at frequency ω .⁸ The application of V_{probe} results in an electrostatic force comprising static (F_{dc}) and dynamic (F_{ω} and $F_{2\omega}$) components as given by Eq. (1), where C'_z and V_{cpd} are the tip-sample capacitance gradient and CPD, respectively,

$$F_{dc} = -\frac{1}{2} C'_z \left[(V_{dc} - V_{cpd})^2 + \frac{1}{2} V_{ac}^2 \right], \quad (1a)$$

$$F_{\omega} = -C'_z (V_{dc} - V_{cpd}) V_{ac} \sin(\omega t), \quad (1b)$$

$$F_{2\omega} = C'_z \frac{1}{4} V_{ac}^2 \cos(2\omega t). \quad (1c)$$

A lock-in amplifier can be used to detect the cantilever's oscillation in response to F_{ω} and $F_{2\omega}$ in terms of amplitude (A_{ω} and $A_{2\omega}$) and phase (θ_{ω} and $\theta_{2\omega}$).

B. Traditional KPFM

According to Eq. 1(b), the first harmonic amplitude response, A_{ω} , is linearly dependent on the applied DC bias. In traditional KPFM, A_{ω} is minimized by a feedback loop that controls the DC bias such that $V_{dc} = V_{cpd}$.⁸ A schematic of the experimental setup for traditional KPFM is shown in Fig. 1(a). From Eq. 1(b), the condition when $V_{dc} = V_{cpd}$ should be independent of V_{ac} and C'_z . In practice however, $1/V_{ac}$ and C'_z dependencies are often observed.^{7,27,29} In fact, the CPD values determined using traditional KPFM are influenced by a variety of factors: Instrumentation effects include electronic offsets and cross talk (between V_{ac} and the photodetector output and/or between V_{ac} and the piezoactuator),^{4,7,35,38} thermomechanical and electrical noise sources,^{39,40} the choice of feedback gains,^{26,27} the choice of V_{ac} frequency, and lock-in amplifier phase offset.^{7,14,28,29} The net effect of these factors is that the input signal to the feedback loop contains contributions, which are not associated with the electrostatic tip-sample forces. Under these conditions, the feedback loop will attempt to minimize a mixed signal leading to an error in the measured CPD value. This cumulative *feedback effect* can be minimized through careful calibration of electronic offsets in instrumentation, the use of shielded electronic cabling, and/or active cross talk compensation.²⁸ The result of the *feedback effect* is that CPD values determined using traditional KPFM may be offset by up to ~ 1 V, depending on the instrumentation and experimental parameters used²⁸ and often manifest as distance dependence,^{7,27,29–31,41} topography cross talk,^{32–34} and a $1/V_{ac}$ dependence due to the influence of the capacitance gradient, C'_z .^{7,27,29}

C. DH-KPFM

DH-KPFM has emerged as a promising technique, both to minimize the influence of the *feedback effect* on measured CPD values and to enable the study of voltage sensitive materials and interactions at the solid-liquid interface. Initially implemented in ultra-high vacuum by Takeuchi *et al.*,⁹ the method was extended to liquid by Kobayashi *et al.*¹⁰ and to ambient environments by Collins *et al.*¹⁵ A schematic of the experimental setup for DH-KPFM is shown in Fig. 1(b). In DH-KPFM, CPD is determined by measuring both A_{ω} and $A_{2\omega}$,

$$A_{\omega} = G_{\omega} |F_{\omega}| = G_{\omega} |C'_z V_{cpd}| V_{ac}, \quad (2a)$$

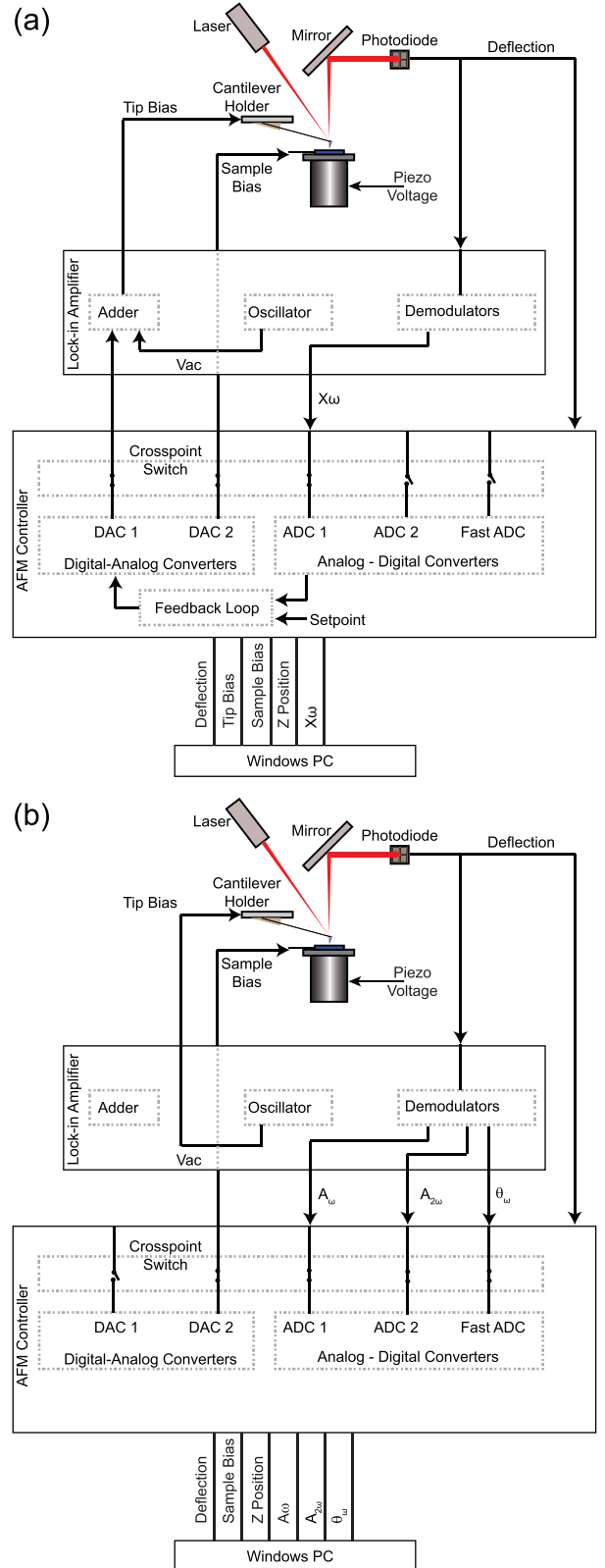


FIG. 1. Schematic of the experimental setup for (a) traditional KPFM and (b) DH-KPFM depicting the signal pathways, AFM controller, lock-in amplifier, and various ADCs and DACs used to collect and generate signals.

$$A_{2\omega} = G_{2\omega} |F_{2\omega}| = G_{2\omega} \left| C'_z \right| \frac{V_{ac}^2}{4}, \quad (2b)$$

$$V_{cpd} = \frac{A_{\omega} \cos(\theta_{\omega})}{A_{2\omega}} \frac{V_{ac}}{4X_{gain}}, \quad (2c)$$

where G_ω and $G_{2\omega}$ are the gains due to the cantilever transfer function at ω and 2ω , respectively, and $X_{\text{gain}} = G_\omega/G_{2\omega}$. Thus, V_{cpd} can be determined using DH-KPFM when X_{gain} , A_ω , $A_{2\omega}$, and θ_ω are known. X_{gain} can be calculated using the equation for a simple harmonic oscillator,¹¹

$$G(\omega) = \frac{1}{k} \frac{1}{\sqrt{[1 - (\omega/\omega_0)^2]^2 + [\omega/Q\omega_0]^2}}. \quad (3)$$

Electronic offsets and electronic cross talk, if present, can also affect CPD values determined by DH-KPFM.^{7,35} However, since there is no feedback loop present in DH-KPFM, there is no error associated with loop gains or trying to minimize a mixed signal (i.e., the *feedback effect*).^{4,35}

III. EXPERIMENTAL DETAILS

A. Experimental setup

A MFP-3D AFM (Asylum Research, an Oxford Instruments Company, USA) and a HF2LI (Zurich Instruments, Switzerland) lock-in amplifier were used for all measurements. All measurements were performed using Pt/Ir-coated MikroMasch DPE18 AFM probes, having nominal resonant frequency, $\omega_0 = 75$ kHz, and stiffness, $k = 3.5$ N/m, with $V_{\text{ac}} = 2$ V (12.5 kHz) applied to the probe (off-resonance). To remove any possible contamination,^{42,43,53} probes were consecutively rinsed in ethanol, isopropanol, and de-ionized water (milliQ, Gradient A10, resistance of 18.2 M Ω cm) and dried under a dry nitrogen flow before being exposed to UV ozone (UV ozone cleaner—ProCleaner™ Plus, BioForce Nanosciences, USA) for 30 min. The sample was a freshly cleaved HOPG surface. Electronics were calibrated using a semi-automated procedure written in IGOR Pro (Wavemetrics, USA). Using a digital multimeter (Agilent Technologies, 34410A), we first calibrated one of the digital to analog converters (DAC) of the AFM controller as a reference and then calibrated all remaining signal pathways. To measure the bandwidth, we applied a chirp function to the sample and measured the resulting CPD, computing the cross correlation between drive and response. Standard uncertainty propagation rules were applied to all results unless otherwise stated. Uncertainties include the uncertainty of all electronic component calibrations as well as the noise associated with the signals measured. Uncertainties are reported as \pm one standard deviation.

B. Automated data collection procedure

An automated data collection procedure was used to interleave the collection of traditional KPFM and DH-KPFM data as a function of tip-sample separation and bias (Fig. 2). For each combination of distance (8 points from 25 nm to 3.0 μm) and applied bias (13 points from -1.5 V to 1.5 V with a step size of 250 mV), a contact mode force curve (10 nN setpoint force and 0.5 Hz rate) with no bias applied was used to reposition the probe. For each tip-sample distance, the CPD was determined using traditional KPFM and DH-KPFM consecutively by sampling for 5 s at a fixed tip-sample separation at a rate of 10 kHz using $V_{\text{ac}} = 2$ V (12.5 kHz) and fitting the respective bias vs. CPD curves at each distance.

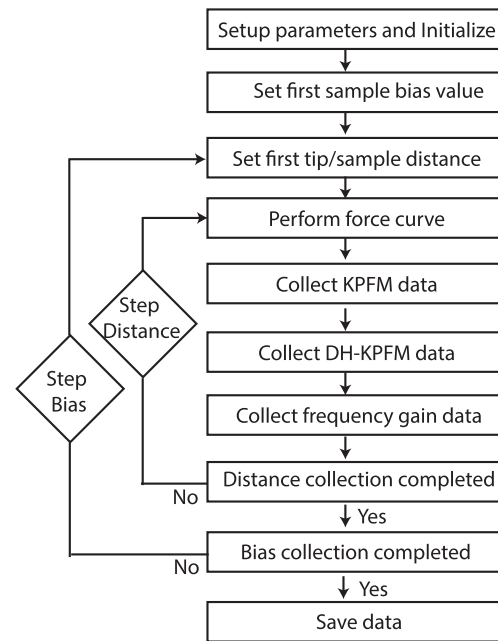


FIG. 2. Flow chart of automated data collection procedure used for collection CPD data using traditional KPFM and DH-KPFM and frequency gain, all as function of bias and tip-sample separation.

For DH-KPFM data sets, the frequency gain at each distance was also determined (see Sec. IV E).

IV. RESULTS AND DISCUSSION

A. Electronic cross talk measurement

In order to check for the presence of electronic cross talk⁴ between the tip bias signal path and the photodiode signal path, an AC bias was applied to the tip bias line at an amplitude of 10 V (12.5 and 25 kHz) with the laser focused on the cantilever chip. The photodiode signal was then analyzed by using the lock-in amplifier at ω and 2ω consecutively, and no signal was detected (estimated noise floor ~ 0.1 mV). This therefore eliminated the need to account for cross talk between these signals. Another possible source of electronic cross talk is between the tip bias signal path and the piezoactuation signal path, which could induce a mechanical oscillation of the cantilever at ω . Again, a signal of 10 V (12.5 and 25 kHz) was applied to the tip bias signal path, and the output of the photodiode with the laser focused on the cantilever chip was analyzed by using the lock-in amplifier at ω and 2ω consecutively, and no signal was detected (estimated noise floor ~ 0.1 mV). This procedure was repeated after removing the circuit board and piezo-stack from the tip holder, and no difference was observed (estimated noise floor ~ 0.1 mV). These observations conclusively rule out the presence of any detectable cross talk in this commercial system, and as such additional shielding and/or compensation schemes were not required for our system.³⁵

B. Electronic offset calibration and corrections

As discussed above, any electronic offsets in instrumentation may lead to the measurement of incorrect CPD values.

To minimize these influences, it is necessary to calibrate all electronic pathways outlined in Fig. 1. Here we chose to correct for not only the DC offset value of each component but also any deviations that may occur as a function of the signal magnitude. To this end, both the linear slope and the offset of each component were determined by fitting the data collected in a semi-automated manner. This procedure constructs a look-up table of linear correction coefficients (Table I) and subsequently allows for correction of data offline during analysis. Note that electronic offsets vary between systems. While electronic offsets of a few tens of mV have been reported for other setups,²⁶ in line with values reported here, electronic offsets for each AFM system will be unique and may also change with time. In order to correct for electronic offsets, each AFM system must be individually characterized.

C. Traditional KPFM optimization

Quantitative traditional KPFM requires feedback loop optimization as the choice of feedback loop parameters will ultimately determine accuracy, stability, and bandwidth of operation.¹¹ The tuning procedure outlined by Jacobs *et al.*²⁶ was implemented in this work, wherein a square wave (typically 300 mV with a frequency of 0.5 Hz) was applied to the HOPG surface. For gain optimization, the in-phase component signal, X_ω , was used as the input to the proportional-integral (PI) feedback loop of the AFM controller.

D. Setpoint correction

The presence of an offset on the analog to digital converter (ADC offset) that provides the error signal (X_ω) to the feedback loop also contributes to the *feedback effect*. In the case where all other artefacts are absent, and the amplitude measured at ω purely arises from electrostatic tip-sample interactions, this ADC offset results in $V_{dc} \neq V_{cpd}$. In our case, a real-time correction of the ADC offset in the error signal was not possible. Fortunately, as the shift in the error signal is constant, it is possible to satisfy the $V_{dc} = V_{cpd}$ condition by choosing an appropriate non-zero feedback setpoint. By ramping the setpoint value, the true minimization of X_ω can be observed (Fig. 3) when the setpoint is equal to the negative value of the offset of ADC1 measured for our setup (Table I). By using a setpoint of

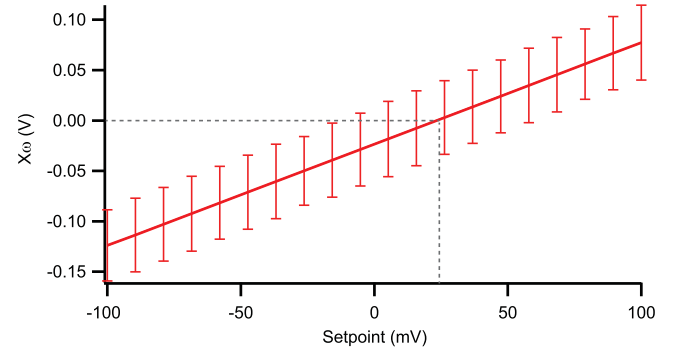


FIG. 3. Measured X_ω as a function of setpoint. The true $X_\omega = 0$ condition is observed when the setpoint is 23.27 mV. Note that the calibrated ADC1 offset = $-23.27 \pm 7 \times 10^{-7}$ mV.

23.27 mV (canceling the measured ADC1 offset), the electrostatic force of the tip-sample interaction is at the true minimum for the experiment and this allows for an accurate value of CPD to be determined. We will show later that this correction also removes the dependency of the CPD on the tip-sample distance and applied bias.

E. DH-KPFM

Quantitative DH-KPFM requires knowledge of the cantilever transfer function and thereby X_{gain} . Whilst X_{gain} can be calculated using Eq. (3), this assumes that the transfer function of the cantilever is free from instrumentation artefacts and that X_{gain} is independent of the tip-sample separation. Here we adopt an approach where we measured X_{gain} directly at each tip-sample separation and applied bias by recording A_ω with excitation at ω and 2ω , consecutively.^{7,13,44} Other approaches based on half-harmonic excitation,¹³ resonance tracking,⁴⁵ band excitation,^{7,13,14,46} or G-mode^{19,20,47,48} may also be used to determine X_{gain} . Figure 4(a) shows the thermal spectra at a tip-sample separation of $\sim 3 \mu\text{m}$ with excitation A_ω applied at 12.5 kHz. The measured $X_{gain} = 0.85 \pm 0.02$ does not show a significant tip-sample distance dependence [Fig. 4(b)] or surface bias dependence [Fig. 4(c)] and is consistently $\sim 10\%$ lower than the calculated X_{gain} ($0.95 \pm 1 \times 10^{-6}$).

F. Bandwidth comparison

In order to compare the bandwidth of traditional KPFM and DH-KPFM, we evaluated the response of the system to a chirp excitation applied to the sample using a cross correlation calculation and measurement of the frequency response at -3 dB. The effective bandwidth of the DH-KPFM was determined to be 53 Hz in comparison with 5.6 Hz for traditional KPFM. The bandwidth for traditional KPFM is limited by the time constant of the lock-in amplifier (900 μs) and the feedback loop settings derived from the tuning procedure outlined by Jacobs *et al.*²⁶ Further improvements in the bandwidth of traditional KPFM may be possible using modern all digital feedback controllers and/or alternative feedback loop tuning strategies. The bandwidth for DH-KPFM is also determined by the time constant of the lock-in amplifier ($\omega_1 = 900 \mu\text{s}$, $\omega_2 = 9.5$ ms). Note that whilst the use of

TABLE I. Look-up table of parameters obtained from instrument calibration.

Component	Slope	Offset (mV)	
DAC 1	$0.982 \pm 2 \times 10^{-6}$	-46.930 ± 0.010	AFM controller
DAC 2	$0.981 \pm 2 \times 10^{-6}$	-60.340 ± 0.008	
ADC 1	$1.007 \pm 2 \times 10^{-7}$	-23.270 ± 0.001	
ADC 2	$1.011 \pm 2 \times 10^{-7}$	-14.890 ± 0.001	
Fast ADC	$1.028 \pm 2 \times 10^{-7}$	-46.220 ± 0.001	
Vac	1.000 ± 0.001	$+0.407 \pm 2.022$	Lock-in amplifier
Adder (DC)	$0.999 \pm 5 \times 10^{-6}$	$+6.895 \pm 0.008$	
Demod (R1)	0.993 ± 0.002	-0.009 ± 0.011	
Demod (R2)	0.997 ± 0.002	-0.007 ± 0.008	
Demod (X1)	0.994 ± 0.002	-0.013 ± 0.011	
Demod (X2)	0.997 ± 0.002	-0.009 ± 0.008	

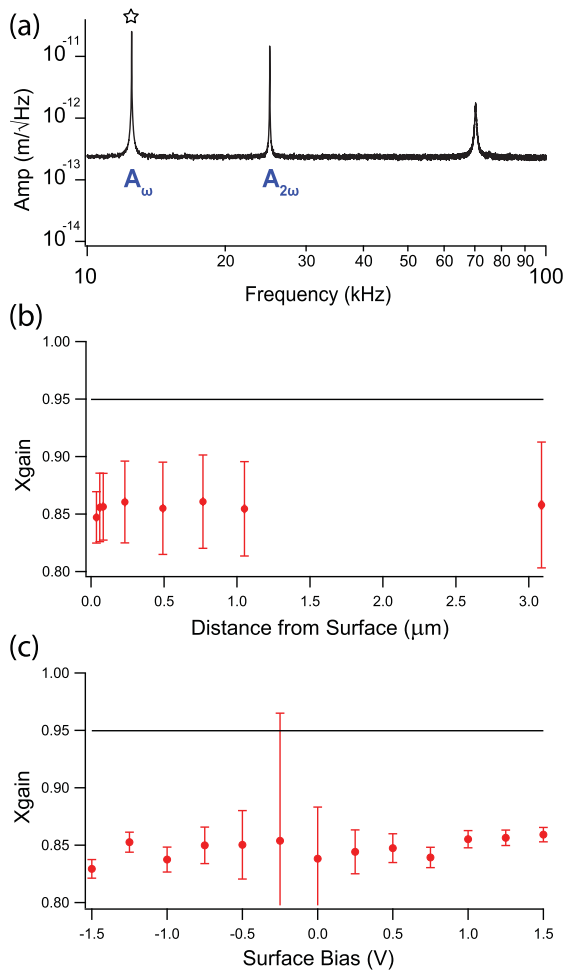


FIG. 4. (a) FFT spectrum of the deflection signal recorded $\sim 3 \mu\text{m}$ from a HOPG surface with $V_{ac} = 2 \text{ V}$ (12.5 kHz). Here we observe the cantilever response at ω (marked with a star) and 2ω , as well as the thermal noise peak at the mechanical resonance frequency of the cantilever. Fitting the mechanical resonance peak results in a measured frequency, quality factor, and spring constant of $\omega_0 = 70\,271.2 \pm 0.7 \text{ Hz}$, $Q = 180.9 \pm 0.7$, and $k = 2.78 \pm 0.16$, respectively. (b) Measured X_{gain} (average = 0.86 ± 0.04) (red markers) as a function of tip-sample separation compared to a calculated X_{gain} (black line) using the parameters determined from (a) and Eq. (3). (c) Measured X_{gain} (average = 0.85 ± 0.02) (red markers) as a function of applied sample bias compared to a calculated X_{gain} (black line). Note that the error bars are larger for biases close to V_{cpd} as the uncertainty in amplitude increases as the signal is minimized.

different time constants for lock-in detection of the 1st and 2nd harmonics are common practice, it may introduce artefacts in the measured CPD for DH-KPFM since C'_Z is detected at a different bandwidth for each harmonic and therefore may no longer be canceled during transients at, e.g., step edges and other boundaries. The bandwidth should be determined

for each experiment, independent of the technique applied, in order to select appropriate scan speeds. The larger bandwidth of DH-KPFM observed here may increase the speed at which accurate measurements can be acquired and aid in the study of charging dynamics in materials and electrical devices.^{47,49–51}

G. Comparison of quantitative traditional KPFM and DH-KPFM

We now examine the surface potential values obtained from traditional KPFM and DH-KPFM in air above a freshly cleaved HOPG surface as a function of applied bias and tip-sample separation. First, we compare the values obtained from an uncalibrated system where we observed a CPD value of $270 \pm 4 \text{ mV}$ for traditional KPFM compared to a value of $197 \pm 8 \text{ mV}$ for DH-KPFM ($\sim 34\%$ or 73 mV difference). It is worth noticing the significant distance and bias dependence (“Dist” and “Vdc Sens,” respectively, in Table II) of the traditional KPFM data compared to the DH-KPFM data (Table II). Applying corrections for electronic offsets (Table I) in the system reduces the observed CPD for traditional KPFM and DH-KPFM to $225 \pm 4 \text{ mV}$ and $190 \pm 8 \text{ mV}$, respectively ($\sim 17\%$ or 45 mV difference), and minimizes the dc bias dependence of the traditional KPFM data, but the distance dependence remains significant. Furthermore, by applying the setpoint correction, the traditional KPFM CPD value reduces to $189 \pm 4 \text{ mV}$, which corresponds to a deviation smaller than the error margin ($\sim 1\%$ difference) of the corrected DH-KPFM CPD value. Under these conditions, the traditional KPFM values exhibit no significant bias or distance dependence. Therefore, in the absence of cross talk, with offset and setpoint correction applied, we have demonstrated that the CPD values measured with traditional KPFM and DH-KPFM agree within the margin of error. We would like to point out that the corrections applied to DH-KPFM changed the CPD values by only 10 mV , once again showing that this technique is less prone to instrumentation artefacts. This combined with the improved bandwidth of DH-KPFM provides more evidence for the utility of open-loop techniques for characterization of surface potential. We attribute the larger uncertainty of the DH-KPFM CPD to a combination of uncertainty in the measured X_{gain} and the noise in the A_ω and $A_{2\omega}$ signals. Figure 5 shows the effect of the corrections for offset and setpoint for traditional KPFM and offset corrections for DH-KPFM.

In order to demonstrate quantitative imaging of a heterogeneous sample, a silicon surface with a $\sim 20 \text{ nm}$ gold film covering approximately half of the scan area was measured

TABLE II. Comparison of uncorrected, electronic offset corrected, and electronic offset + setpoint corrected traditional KPFM and DH-KPFM data.

Technique	No corrections			Electronic offset corrections			Electronic offset + setpoint corrections		
	CPD (mV)	Vdc Sens (%)	Dist Sens (mV/μm)	CPD (mV)	Vdc Sens (%)	Dist Sens (mV/μm)	CPD (mV)	Vdc Sens (%)	Dist Sens (mV/μm)
Traditional KPFM	270 ± 4	2.6 ± 0.4	12 ± 2	225 ± 4	0.7 ± 0.4	12 ± 2	189 ± 4	0.6 ± 0.4	-1 ± 2
DH-KPFM	198 ± 8	2 ± 1	1 ± 3	190 ± 8	1 ± 1	-1 ± 4	190 ± 8	1 ± 1	-1 ± 4
% difference	33.5	16.7	1.0

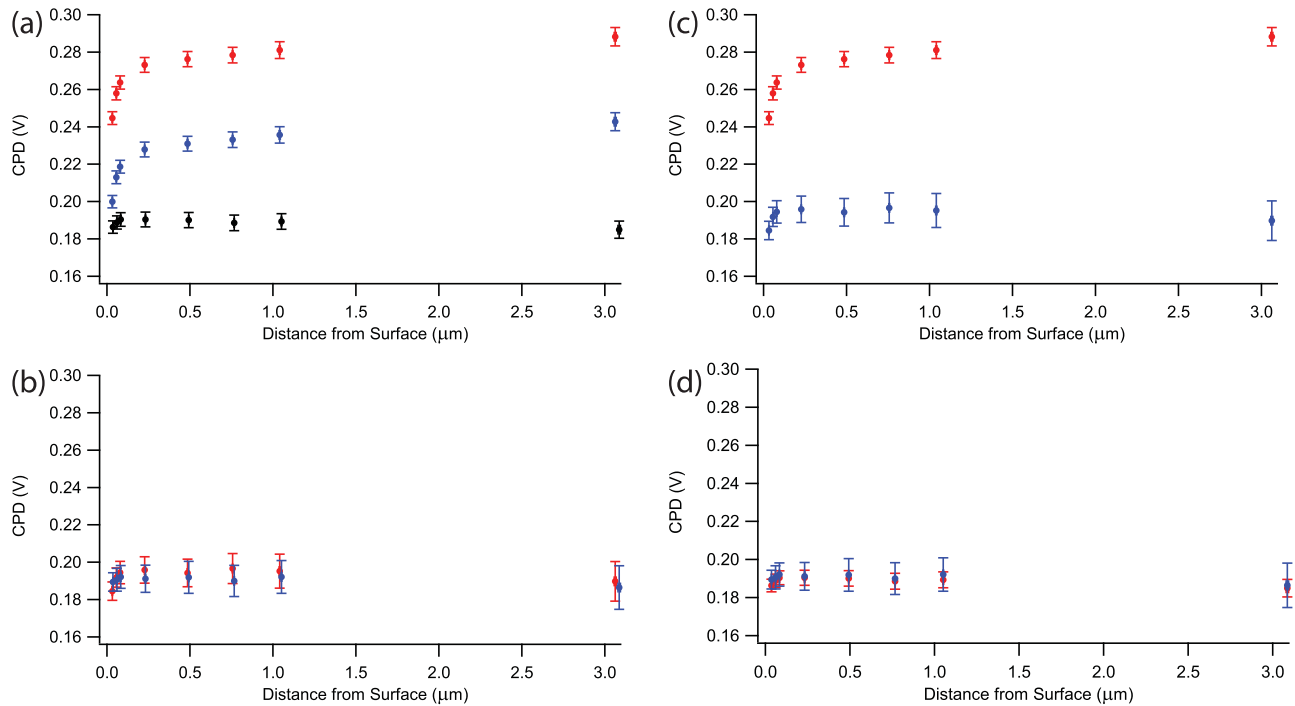


FIG. 5. CPD measurements obtained using traditional KPFM and DH-KPFM as a function of tip-sample separation. (a) Comparison of traditional KPFM measurements: uncorrected (red), offset corrected (blue), and offset + setpoint corrected (black). (b) Comparison of DH-KPFM measurements: uncorrected (red) and corrected (blue). (c) Uncorrected traditional KPFM (red) and uncorrected DH-KPFM (blue). (d) Corrected traditional KPFM and corrected DH-KPFM. $V_{ac} = 2$ V (12.5 kHz).

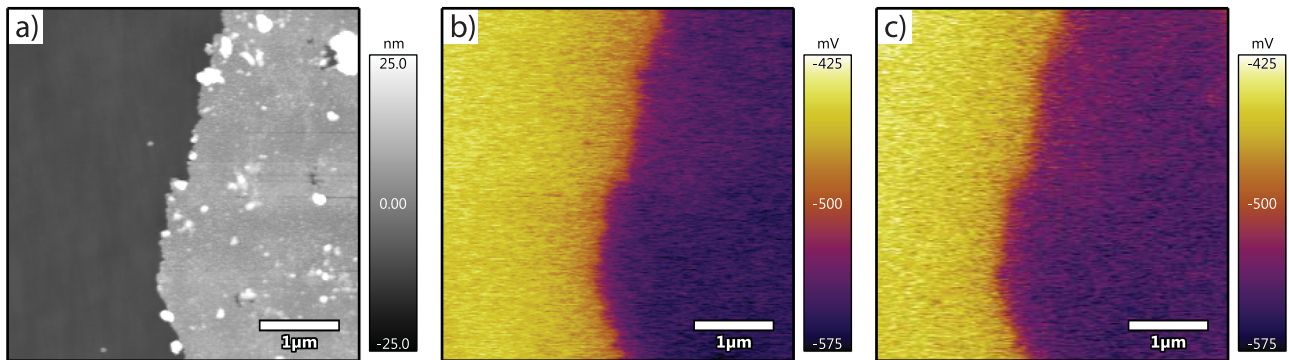


FIG. 6. Imaging a silicon surface with a ~ 20 nm gold film. (a) Topography, (b) corrected traditional KPFM, and (c) corrected DH-KPFM. $V_{ac} = 4$ V (12.5 kHz).

using traditional KPFM and DH-KPFM. We found good agreement between the two techniques when scanning the same area (Fig. 6). The difference in measured CPD between

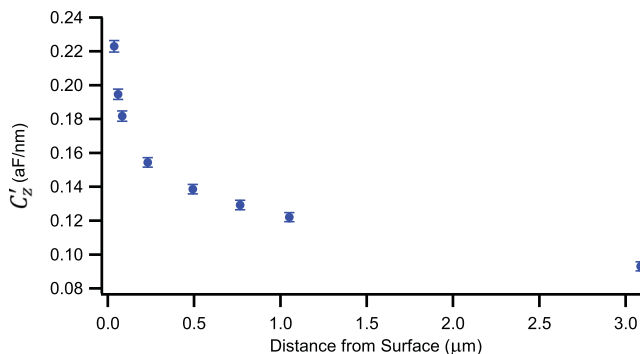


FIG. 7. Measurement of the capacitance gradient as a function of tip-sample separation using corrected DH-KPFM. $V_{ac} = 2$ V (12.5 kHz).

Figs. 6(b) and 6(c) was found to be 4.0 ± 10.4 mV (20% of images excluded from analysis due to drift).

DH-KPFM also allows the capacitance gradient to be measured as a function of tip-sample distance, as shown in Fig. 7. Here the capacitance gradient is determined by $C'_z = \frac{A_{2\omega} 4k}{V_{ac}^2}$. Gramse *et al.* have previously shown that such data can be fit with a model describing the geometry of the probe in order to extract the dielectric constant of the tip-sample interaction.⁵² Such measurements could also be made whilst using traditional KPFM if $A_{2\omega}$ is also recorded.

V. CONCLUSION

We have examined the quantitative agreement between traditional KPFM (CL-KPFM) and DH-KPFM (OL-KPFM). We have shown that DH-KPFM allows for higher bandwidth of operation and that it is more robust to electronic offsets that

may be present in a given AFM system. By carefully measuring and applying corrections for offsets and applying a new “setpoint correction,” we were able to show that DH-KPFM and traditional KPFM agree within 1% for a calibrated system. Furthermore, the addition of the “setpoint correction” resulted in the removal of both bias and tip-sample separation dependence in CPD values for traditional KPFM operation. We also demonstrated quantitative agreement when imaging a heterogeneous sample as well as illustrating the potential for the measurement of dielectric constants.

ACKNOWLEDGMENTS

This publication has emanated from research conducted with financial support from UCD Research, the Alexander von Humboldt Foundation and Science Foundation, Ireland (07/IN1/B931, 12/IA/1449, 14/IFB/2711, 14/US/I3113, 15/IFB/3570, 17/CDA/4637). A portion of this research was conducted at the Center for Nanophase Materials Sciences, which is a DOE Office of Science User Facility. The authors are grateful to S. P. Jarvis for insightful discussions. This manuscript has been authored by UT -Battelle, LLC under Contract No. DE-AC05-00OR22725 with the U.S. Department of Energy. The United States Government retains and the publisher, by accepting the article for publication, acknowledges that the United States Government retains a non-exclusive, paid-up, irrevocable, world-wide license to publish or reproduce the published form of this manuscript, or allow others to do so, for United States Government purposes. The Department of Energy will provide public access to these results of federally sponsored research in accordance with the DOE Public Access Plan (<http://energy.gov/downloads/doe-public-access-plan>).

- ¹C. Sommerhalter, T. W. Matthes, T. Glatzel, A. Jäger-Waldau, and M. C. Lux-Steiner, “High-sensitivity quantitative Kelvin probe microscopy by noncontact ultra-high-vacuum atomic force microscopy,” *Appl. Phys. Lett.* **75**, 286–288 (1999).
- ²U. Zerweck, C. Loppacher, T. Otto, S. Grafström, and L. M. Eng, “Accuracy and resolution limits of Kelvin probe force microscopy,” *Phys. Rev. B* **71**, 125424 (2005).
- ³H. Sugimura, Y. Ishida, K. Hayashi, O. Takai, and N. Nakagiri, “Potential shielding by the surface water layer in Kelvin probe force microscopy,” *Appl. Phys. Lett.* **80**, 1459–1461 (2002).
- ⁴S. Barbet *et al.*, “Cross-talk artefacts in Kelvin probe force microscopy imaging: A comprehensive study,” *J. Appl. Phys.* **115**, 144313 (2014).
- ⁵C. B. Jacobs *et al.*, “UV-activated ZnO films on a flexible substrate for room temperature O₂ and H₂O sensing,” *Sci. Rep.* **7**, 6053 (2017).
- ⁶S. V. Kalinin and D. A. Bonnell, “Local potential and polarization screening on ferroelectric surfaces,” *Phys. Rev. B* **63**, 125411 (2001).
- ⁷L. Collins *et al.*, “Open loop Kelvin probe force microscopy with single and multi-frequency excitation,” *Nanotechnology* **24**, 475702 (2013).
- ⁸M. Nonnenmacher, M. P. O’Boyle, and H. K. Wickramasinghe, “Kelvin probe force microscopy,” *Appl. Phys. Lett.* **58**, 2921–2923 (1991).
- ⁹O. Takeuchi, Y. Ohrai, S. Yoshida, and H. Shigekawa, “Kelvin probe force microscopy without bias-voltage feedback,” *Jpn. J. Appl. Phys., Part 1* **46**, 5626 (2007).
- ¹⁰N. Kobayashi, H. Asakawa, and T. Fukuma, “Nanoscale potential measurements in liquid by frequency modulation atomic force microscopy,” *Rev. Sci. Instrum.* **81**, 123705 (2010).
- ¹¹N. Kobayashi, H. Asakawa, and T. Fukuma, “Quantitative potential measurements of nanoparticles with different surface charges in liquid by open-loop electric potential microscopy,” *J. Appl. Phys.* **110**, 044315 (2011).

- ¹²N. Kobayashi, H. Asakawa, and T. Fukuma, “Dual frequency open-loop electric potential microscopy for local potential measurements in electrolyte solution with high ionic strength,” *Rev. Sci. Instrum.* **83**, 033709 (2012).
- ¹³S. Guo, S. V. Kalinin, and S. Jesse, “Half-harmonic Kelvin probe force microscopy with transfer function correction,” *Appl. Phys. Lett.* **100**, 063118 (2012).
- ¹⁴S. Guo, S. V. Kalinin, and S. Jesse, “Open-loop band excitation Kelvin probe force microscopy,” *Nanotechnology* **23**, 125704 (2012).
- ¹⁵L. Collins *et al.*, “Dual harmonic Kelvin probe force microscopy for surface potential measurements of ferroelectrics,” in *Applications of Ferroelectrics held jointly with 2012 European Conference on the Applications of Polar Dielectrics and 2012 International Symp Piezoresponse Force Microscopy and Nanoscale Phenomena in Polar Materials (ISAF/ECAPD/PFM), 2012 Intl Symp 1–4* (IEEE, 2012).
- ¹⁶L. Collins *et al.*, “Dual harmonic Kelvin probe force microscopy at the graphene–liquid interface,” *Appl. Phys. Lett.* **104**, 133103 (2014).
- ¹⁷L. Collins *et al.*, “Probing charge screening dynamics and electrochemical processes at the solid–liquid interface with electrochemical force microscopy,” *Nat. Commun.* **5**, 3871 (2014).
- ¹⁸Q. Li *et al.*, “Switching spectroscopic measurement of surface potentials on ferroelectric surfaces via an open-loop Kelvin probe force microscopy method,” *Appl. Phys. Lett.* **101**, 242906 (2012).
- ¹⁹L. Collins *et al.*, “Full data acquisition in Kelvin probe force microscopy: Mapping dynamic electric phenomena in real space,” *Sci. Rep.* **6**, 30557 (2016).
- ²⁰L. Collins *et al.*, “G-mode magnetic force microscopy: Separating magnetic and electrostatic interactions using big data analytics,” *Appl. Phys. Lett.* **108**, 193103 (2016).
- ²¹S. Yoshida *et al.*, “Tip-induced band bending and its effect on local barrier height measurement studied by light-modulated scanning tunneling spectroscopy,” *e-J. Surf. Sci. Nanotechnol.* **4**, 192–196 (2006).
- ²²C. Sommerhalter and T. Glatzel, “Kelvin probe force microscopy in ultra high vacuum using amplitude modulation detection of the electrostatic forces,” *Appl. Surf. Sci.* **157**, 263–268 (2000).
- ²³A. L. Domanski *et al.*, “Kelvin probe force microscopy in non-polar liquids,” *Langmuir* **28**, 13892 (2012).
- ²⁴K. Umeda *et al.*, “Practical aspects of Kelvin-probe force microscopy at solid/liquid interfaces in various liquid media,” *J. Appl. Phys.* **116**, 134307 (2014).
- ²⁵K. Honbo *et al.*, “Visualizing nanoscale distribution of corrosion cells by open-loop electric potential microscopy,” *ACS Nano* **10**, 2575–2583 (2016).
- ²⁶H. O. Jacobs, H. F. Knapp, and A. Stemmer, “Practical aspects of Kelvin probe force microscopy,” *Rev. Sci. Instrum.* **70**, 1756 (1999).
- ²⁷H. Diesinger, D. Deresmes, and T. Mélin, “Capacitive crosstalk in AM-mode KPFM,” in *Kelvin Probe Force Microscopy* (Springer Science + Business Media, 2012).
- ²⁸T. Mélin, S. Barbet, H. Diesinger, D. Théron, and D. Deresmes, “Note: Quantitative (artifact-free) surface potential measurements using Kelvin force microscopy,” *Rev. Sci. Instrum.* **82**, 036101 (2011).
- ²⁹Y. Wu and M. A. Shannon, “AC driving amplitude dependent systematic error in scanning Kelvin probe microscope measurements: Detection and correction,” *Rev. Sci. Instrum.* **77**, 043711 (2006).
- ³⁰A. Liscio, V. Palermo, K. Müllen, and P. Samorì, “Tip–sample interactions in Kelvin probe force microscopy: Quantitative measurement of the local surface potential,” *J. Phys. Chem. C* **112**, 17368–17377 (2008).
- ³¹D. S. H. Charrier, M. Kemerink, B. E. Smalbrugge, T. de Vries, and R. A. J. Janssen, “Real versus measured surface potentials in scanning Kelvin probe microscopy,” *ACS Nano* **2**, 622–626 (2008).
- ³²A. Efimov and S. R. Cohen, “Simulation and correction of geometric distortions in scanning Kelvin probe microscopy,” *J. Vac. Sci. Technol., A* **18**, 1051 (2000).
- ³³K. Okamoto, Y. Sugawara, and S. Morita, “The elimination of the “artifact” in the electrostatic force measurement using a novel noncontact atomic force microscope/electrostatic force microscope,” *Appl. Surf. Sci.* **188**, 381–385 (2002).
- ³⁴M. Lee, W. Lee, and F. B. Prinz, “Geometric artefact suppressed surface potential measurements,” *Nanotechnology* **17**, 3728 (2006).
- ³⁵L. Polak, S. de Man, and R. J. Wijngaarden, “Note: Switching crosstalk on and off in Kelvin probe force microscopy,” *Rev. Sci. Instrum.* **85**, 046111 (2014).
- ³⁶L. Kou *et al.*, “Surface potential imaging with atomic resolution by frequency-modulation Kelvin probe force microscopy without bias voltage feedback,” *Nanotechnology* **26**, 195701 (2015).

- ³⁷L. Collins, J. I. Kilpatrick, S. V. Kalinin, and B. J. Rodriguez, "Towards nanoscale electrical measurements in liquid by advanced KPFM techniques: A review," *Rep. Prog. Phys.* **81**, 086101 (2018).
- ³⁸O. Vatel and M. Tanimoto, "Kelvin probe force microscopy for potential distribution measurement of semiconductor devices," *J. Appl. Phys.* **77**, 2358 (1995).
- ³⁹H.-J. Butt and M. Jaschke, "Calculation of thermal noise in atomic force microscopy," *Nanotechnology* **6**, 1–7 (1999).
- ⁴⁰C. A. J. Putman, B. G. De Grooth, N. F. Van Hulst, and J. Greve, "A detailed analysis of the optical beam deflection technique for use in atomic force microscopy," *J. Appl. Phys.* **72**, 6–12 (1992).
- ⁴¹L. Collins *et al.*, "Quantitative 3D-KPFM imaging with simultaneous electrostatic force and force gradient detection," *Nanotechnology* **26**, 175707 (2015).
- ⁴²Y. Lo, N. Huefner, W. Chan, and P. Dryden, "Organic and inorganic contamination on commercial AFM cantilevers," *Langmuir* **15**, 6522–6526 (1999).
- ⁴³E. Bonaccorso and G. Gillies, "Revealing contamination on AFM cantilevers by microdrops and microbubbles," *Langmuir* **20**, 11824–11827 (2004).
- ⁴⁴Y. Kim *et al.*, "Nonlinear phenomena in multiferroic nanocapacitors: Joule heating and electromechanical effects," *ACS Nano* **5**, 9104–9112 (2011).
- ⁴⁵B. J. Rodriguez, C. Callahan, S. V. Kalinin, and R. Proksch, "Dual-frequency resonance-tracking atomic force microscopy," *Nanotechnology* **18**, 475504 (2007).
- ⁴⁶S. Jesse, S. V. Kalinin, R. Proksch, A. P. Baddorf, and B. J. Rodriguez, "The band excitation method in scanning probe microscopy for rapid mapping of energy dissipation on the nanoscale," *Nanotechnology* **18**, 435503 (2007).
- ⁴⁷L. Collins *et al.*, "Breaking the time barrier in Kelvin probe force microscopy: Fast free force reconstruction using the G-mode platform," *ACS Nano* **11**, 8717–8729 (2017).
- ⁴⁸L. Collins *et al.*, "Multifrequency spectrum analysis using fully digital G mode-Kelvin probe force microscopy," *Nanotechnology* **27**, 105706 (2016).
- ⁴⁹S. D. Collins *et al.*, "Observing ion motion in conjugated polyelectrolytes with Kelvin probe force microscopy," *Adv. Electron. Mater.* **3**, 1700005 (2017).
- ⁵⁰E. Strelcov *et al.*, "Space- and time-resolved mapping of ionic dynamic and electroresistive phenomena in lateral devices," *ACS Nano* **7**, 6806–6815 (2013).
- ⁵¹J. L. Garrett *et al.*, "Real-time nanoscale open-circuit voltage dynamics of perovskite solar cells," *Nano Lett.* **17**, 2554–2560 (2017).
- ⁵²G. Gramse, G. Gomila, and L. Fumagalli, "Quantifying the dielectric constant of thick insulators by electrostatic force microscopy: Effects of the microscopic parts of the probe," *Nanotechnology* **23**, 205703 (2012).
- ⁵³A. V. Ievlev, C. Brown, M. J. Burch, J. C. Agar, G. A. Velarde, L. W. Martin, P. Maksymovych, S. V. Kalinin, and O. S. Ovchinnikova, "Chemical phenomena of atomic force microscopy scanning," *Anal. Chem.* **90**(5), 3475–3481 (2018).